SMR 1746 - 14

_____

WORKSHOP ON DRIVEN STATES IN SOFT AND BIOLOGICAL MATTER
18 - 28 April 2006
_____

Background Information for Talk on

"Collective Behavior in Addressable Excitable Media"

(Design and Control of Wave Propagation Patterns in excitable Media)

Kenneth SHOWALTER
West Virginia University, Dept. of Chemistry
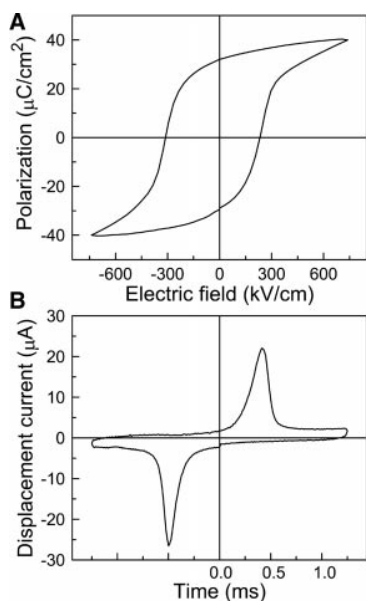*Morgantown, West Virginia 26506, U.S.A.*

Fig. 4. (A) *P-E* hysteresis loop of a Pt-BLT(100)-SrRuO$_3$(110) capacitor ($\alpha_{(100)}$ = 99%). **(B)** Displacement current curve recorded during the *P-E* curve measurement. BLT film thickness is 1 μm.

other domains (twins) have different azimuthal orientations. Figure 3D shows a high-resolution structure image of a thin area of grain "M," showing a good correspondence to the inserted structure model.

Ferroelectric polarization−electric field (*P-E*) hysteresis loops and simultaneously recorded displacement currents of BLT films (thickness 1 μm) with $\alpha_{(100)}$ = 99% were recorded at 200 Hz, as shown in Fig. 4. Platinum top electrodes (diameter 100 μm) were sputter-deposited. The films revealed well-saturated hysteresis loops (Fig. 4A) with a remanent polarization and a coercive field of 32 μC/cm^2 and 265 kV/cm, respectively, for a maximum applied electric field of 740 kV/cm (*18*). The corresponding displacement current curve is shown in Fig. 4B. The polarization corresponds well to the value of 35 μC/cm^2 that can be calculated using the relation between the major polarization values of BLT and Bi$_4$Ti$_3$O$_{12}$ given by Shimakawa *et al*. (*27*) and the polarization value of Bi$_4$Ti$_3$O$_{12}$ single crystals given by Cummins and Cross (*14*).

One of the proposed mechanisms for the absence of fatigue in bismuth-layered perovskite films is related to a space-charge compensation near the electrodes by the bismuth oxide double layers (*1*). However, the space-charge compensation is likely to be difficult in films having their Bi$_2$O$_2$ planes perpendicular to the film plane. Initial fatigue characterization up to 10^9 cycles (fig. S1) (*28*) shows hardly any fatigue. For actual applications in memory devices, the absence of fatigue in the range of 10^9 to 10^{12} switching cycles will be essential.

References and Notes
1. C. A. P. de Araujo, J. D. Cuchiaro, L. D. McMillan, M. C. Scott, J. F. Scott, *Nature* **374**, 627 (1995).
2. B. H. Park *et al.*, *Nature* **401**, 682 (1999).
3. A. Gruverman, *Appl. Phys. Lett.* **75**, 1452 (1999).
4. R. Ramesh *et al.*, *Science* **252**, 944 (1991).
5. J. Lettieri *et al.*, *Appl. Phys. Lett.* **76**, 2937 (2000).
6. H. N. Lee *et al.*, *J. Appl. Phys.* **88**, 6658 (2000).
7. H. N. Lee, D. N. Zakharov, S. Senz, A. Pignolet, D. Hesse, *Appl. Phys. Lett.* **79**, 2961 (2001).
8. H. N. Lee, D. N. Zakharov, P. Reiche, R. Uecker, D. Hesse, *Mater. Res. Symp. Proc.* **688**, C8.5 (2002).
9. S. Y. Wu, W. J. Takei, M. H. Francombe, S. E. Cummins, *Ferroelectrics* **3**, 217 (1972).
10. C. D. Theis *et al.*, *Appl. Phys. Lett.* **72**, 2817 (1998).
11. K. Ishikawa, H. Funakubo, *Appl. Phys. Lett.* **75**, 1970 (1999).
12. S. E. Moon *et al.*, *Appl. Phys. Lett.* **75**, 2827 (1999).
13. A. D. Rae, J. G. Thompson, R. L. Withers, A. C. Willis, *Acta Crystallogr.* **B46**, 474 (1990).
14. S. E. Cummins, L. E. Cross, *J. Appl. Phys.* **39**, 2268 (1968).
15. H. N. Lee *et al.*, *Appl. Phys. A* **71**, 101 (2000).
16. H. N. Lee *et al.*, *Appl. Phys. Lett.* **77**, 3260 (2000).
17. H. N. Lee, D. Hesse, *Appl. Phys. Lett.* **80**, 1040 (2002).
18. In this paper, *a-b* growth twins are not explicitly considered. The difference between the lattice parameters *a* and *b* of BLT is so small that it is difficult to discriminate between them. However, the high value of the remanent polarization of our films implies that there are almost no *a-b* twins present or that the latter are totally switched into the *a*-axis orientation.
19. S. Y. Hou, J. Kwo, R. K. Watts, J. Y. Cheng, D. K. Fork, *Appl. Phys. Lett.* **67**, 1387 (1995).
20. Although this high growth temperature most probably does not comply with memory device fabrication, it can probably be reduced by using other oxidants instead of O$_2$, including nitrous oxide (N$_2$O) or nitrogen dioxide (NO$_2$) (*29, 30*).
21. C. Girault, D. Damiani, J. Aubreton, A. Catherinot, *Appl. Phys. Lett.* **55**, 182 (1989).
22. D. B. Geohegan, *Appl. Phys. Lett.* **60**, 2732 (1992).
23. K. Kanehori, F. Kirino, Y. Ito, K. Miyauchi, T. Kudo, *J. Electrochem. Soc.* **136**, 1265 (1989).
24. J. Fujita, T. Yoshitake, A. Kamijo, T. Satoh, H. Igarashi, *J. Appl. Phys.* **64**, 1292 (1988).
25. C. B. Eom, A. F. Marshall, S. S. Laderman, R. D. Jacowitz, T. H. Geballe, *Science* **249**, 1549 (1990).
26. Q. Zhong, P. C. Chou, Q. L. Li, G. S. Taraldsen, A. Ignatiev, *Physica C* **246**, 288 (1995).
27. Y. Shimakawa *et al.*, *Appl. Phys. Lett.* **79**, 2791 (2001).
28. Materials and methods are available as supplementary material on *Science* Online.
29. G. Koren, A. Gupta, R. J. Baseman, *Appl. Phys. Lett.* **54**, 1920 (1989).
30. M. Kanai, K. Horiuchi, T. Kawai, S. Kawai, *Appl. Phys. Lett.* **57**, 2716 (1990).
31. Supported in part by European Union project IST-2000-28495 (INVEST) (H.N.L.) and by the Deutsche Forschungsgemeinschaft via the Group of Researches FOR 404 at Martin Luther University Halle-Wittenberg.

Design and Control of Wave Propagation Patterns in Excitable Media

Tatsunari Sakurai, Eugene Mihaliuk, Florin Chirila, Kenneth Showalter*

Intricate patterns of wave propagation are exhibited in a chemical reaction-diffusion system with spatiotemporal feedback. Wave behavior is controlled by feedback-regulated excitability gradients that guide propagation in specified directions. Waves interacting with boundaries and with other waves are observed when interaction terms are incorporated into the control algorithm. Spatiotemporal feedback offers wide flexibility for designing and controlling wave behavior in excitable media.

It is now possible to implement control strategies that yield new modes of spatiotemporal behavior in excitable chemical and biological media. Feedback methods have been used to control spatiotemporal activity in the Pt-catalyzed oxidation of CO (*1*), suggesting a means for enhancing catalytic efficiencies, and focused laser light has been used to direct wave propagation in this system by thermally altering local catalytic activity (*2*). Pattern formation (*3–5*) and spiral waves (*6, 7*) in the Belousov-Zhabotinsky (BZ) reaction (*8*) have also

been controlled by using feedback techniques, which points to the possibility of regulating spatiotemporal dynamics in excitable biological tissues. A recent advance in this direction is the control of seizure-like events in hippocampal brain slices with adaptive electric fields (*9*). The ability to manipulate spatiotemporal behavior provides both a means of generating desired dynamical patterns and the tools for probing underlying mechanisms.

Here, we describe the implementation of control methods that yield particle-like waves that propagate in, effectively, user-defined patterns. Unstable waves in the photosensitive BZ reaction (*10*) are stabilized by global feedback that affects the overall excitability of the medium (*11*), and the motion of these

Department of Chemistry, West Virginia University, Morgantown, WV 26506, USA.

*To whom correspondence should be addressed. E-mail: kshowalt@wvu.edu

waves is controlled by imposing excitability gradients that are regulated by a secondary feedback loop. We present experimental realizations and numerical simulations that demonstrate unprecedented control of spatiotemporal wave activity.

We carried out experiments using a photosensitive BZ medium that was monitored with a video camera and illuminated with a computer-controlled video projector. A thin layer of silica gel (0.3 mm $\times$ 20 mm $\times$ 30 mm) containing immobilized ruthenium(II)-bipyridyl, a light-sensitive catalyst for the BZ reaction, was cast onto a microscope slide. This gel was bathed in continually refreshed catalyst-free solution so that a particular nonequilibrium state could be maintained for study (12, 13).

Images of the waves were captured with a video camera and processed by a computer in real time to return control images to the gel via the video projector. The excitability of the medium is determined by the photochemical production of bromide ion (14, 15), and, hence, a desired excitability at each pixel could be imposed by the illumination intensity (16). A new illumination pattern was calculated for every iteration, according to the following control algorithm:

$$\phi(x, y) = aA + b + cG(x, y)$$
$$A = \sum_{x,y} \Theta \left[p(x, y) - p_{th} \right]$$
(1)

where $\phi(x, y)$ is the output image to the projector and $p(x, y)$ is the input image from the video camera. The wave area (A) is defined as the region containing the oxidized ruthenium catalyst [$Ru(bpy)_3^{3+}$] and is obtained by counting the video image pixels with a gray level $p(x, y)$ above the threshold p_{th}, where Θ is the Heaviside function giving 0 or 1 in the summation (12). The gain a and offset b define the primary feedback loop, which increases or decreases the excitability of the medium as the wave becomes smaller or larger, respectively, thus stabilizing the wave size. The term $G(x, y)$, with gain c, represents the small variation in light intensity imposed to direct the motion of the wave

according to a secondary feedback loop, different implementations of which are presented below. Two or more waves can be independently controlled, each with its own feedback loop, by localizing the feedback around each wave.

Different realizations of G give rise to different patterns of wave motion. In the simple case of a radially symmetrical distribution, $G(r) = ln(r) - ln(r_m)$, the motion of a wave resembles that of a particle in a potential field (17). To minimize the effect of directional control on the wave size, the second term, $ln(r_m)$, maintains $G = 0$ at the wave "center of mass." Figure 1 shows the trajectories of three experimental waves, where the initial wave position was slightly varied with respect to the center of the symmetrical gradient. Also shown are three wave trajectories simulated with the Oregonator model for the photosensitive BZ reaction (18–21). The trajectories in both the experiments and simulations would be horizontal in a gradient-free field; however, each is increasingly deflected by the "attracting field." The most highly curved trajectories in Fig. 1, A and B, closely approach the center of the symmetrical gradient.

Much greater flexibility for realizing complex wave trajectories is possible when G is dynamically varied according to the current and target locations of the wave. The direction of wave propagation can be conveniently controlled by using a simple linear gradient applied perpendicular to the direction of propagation at the wave center of mass (12). The wave turns to the left or right, depending on the sign of the gradient, and at a rate that depends on its magnitude. Figure 2 shows examples of wave trajectories in which the gradient is proportional to the deviation of the wave position from a hypotrochoid path (X, Y) computed according to:

$$X = (\alpha - \beta)cos(\theta) + \gamma cos\left[\left(\frac{\alpha}{\beta} - 1 \right) \theta \right]$$

$$Y = (\alpha - \beta)sin(\theta) - \gamma sin\left[\left(\frac{\alpha}{\beta} - 1 \right) \theta \right]$$
(2)

where α, β, and γ are geometric parameters and θ is the independent variable. Simple circular trajectories for $\alpha = \gamma = 0$ are shown in Fig. 2, A and B, whereas other values of these parameters generate three-lobed hypotrochoid trajectories (Fig. 2, C and D) and four-lobed hypotrochoid trajectories (Fig. 2, E and F). Although the trajectories in Fig. 2, C to F, resemble the hypocycloid patterns arising from tracking the tip of meandering spiral waves (22), the wave behavior is distinctly different in character. Rather than the natural meandering found in spiral waves, these patterns arise from controlling waves to follow particular geometric paths (23). Virtually any trajectory can be designed and implemented by incorporating an appropriate function into the control loop, within the limitations imposed by the dynamics of wave propagation in gradients.

Wave propagation akin to Brownian motion is exhibited when random variations in the excitability gradient are imposed at equal time intervals (Fig. 3). Wave trajectories for three different experiments are shown in Fig. 3A, where each realization was started at the
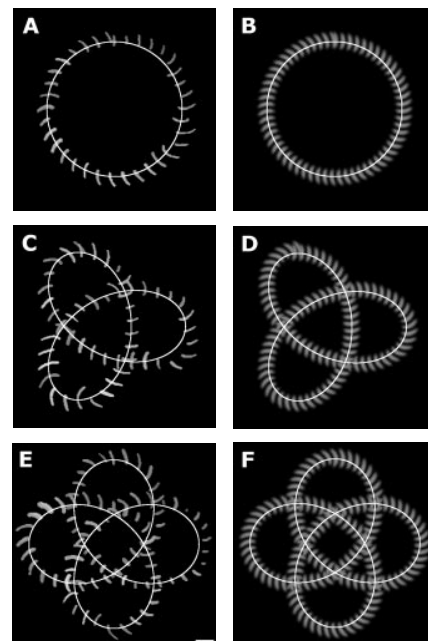
Fig. 2. Hypotrochoid trajectories resulting from controlling wave propagation according to Eqs. 1 and 2. (**A, C,** and **E**) A superposition of snapshots taken every 40.0 s of experimental wave behavior. (**B, D,** and **F**) A superposition of snapshots taken every 0.1 dimensionless time units of simulated wave behavior. The target trajectories (solid curves) were computed from Eq. 2 with the geometric parameters $\alpha = 0, 60, 60$; $\beta = 100, 20, 15$; $\gamma = 0, 80, 80$ in (A) and (B), (C) and (D), and (E) and (F), respectively. The feedback parameters a and b, and the directional gain c, were 0.4, 15.0, and 0.125 in the experiments, and 8.0×10^{-5}, 0.06, and 2.5×10^{-5} in the simulations. The scale bar in (E) is 2.0 mm.
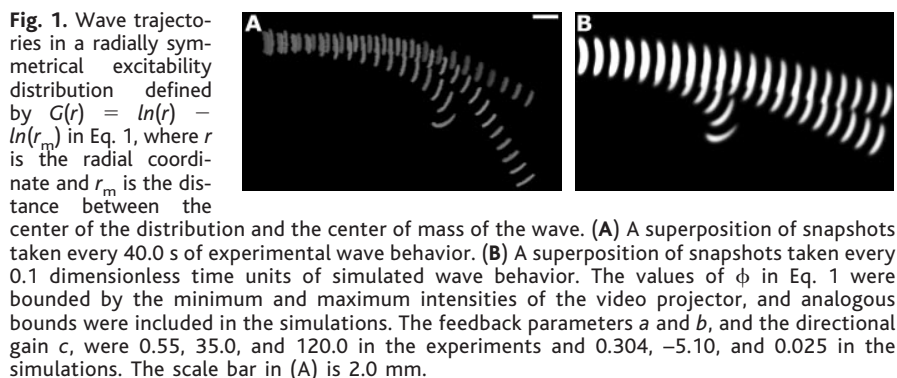
Fig. 1. Wave trajectories in a radially symmetrical excitability distribution defined by $G(r) = ln(r) - ln(r_m)$ in Eq. 1, where r is the radial coordinate and r_m is the distance between the center of the distribution and the center of mass of the wave. (**A**) A superposition of snapshots taken every 40.0 s of experimental wave behavior. (**B**) A superposition of snapshots taken every 0.1 dimensionless time units of simulated wave behavior. The values of ϕ in Eq. 1 were bounded by the minimum and maximum intensities of the video projector, and analogous bounds were included in the simulations. The feedback parameters a and b, and the directional gain c, were 0.55, 35.0, and 120.0 in the experiments and 0.304, −5.10, and 0.025 in the simulations. The scale bar in (A) is 2.0 mm.

same point. The subsequent random variation of the gradient leads to a completely different exploration of the medium in each case. An overlay of snapshots at successive time intervals shows the wave behavior as a function of time for one of the trajectories. Simulated trajectories (Fig. 3B), again with three different realizations, are shown starting at the same point, and the wave behavior for one of the trajectories is shown by an overlay of snapshots. These experiments and simula-

tions represent the simplest possibility for random wave propagation; more complex variations such as biased random walks could be realized by suitably varying G in Eq. 1.

Waves are confined to a designated region of the medium when a boundary rule is incorporated into the control algorithm. Experimental (Fig. 4A) and simulated (Fig. 4B) wave trajectories were confined to the vicinity of a rectangular box, within which the wave propagates in a gradient-free field. When the wave reaches the

Fig. 3. Waves undergoing random walks. (**A**) Experiments were carried out with the gain $c = 1.0$ and the slope of G randomly selected from a uniform probability distribution between −2.5 and 2.5 every 20.0 s, which was also the interval between the superimposed snapshots. Three different random walk trajectories, showing the wave midpoint as a function of time for the same starting point, are shown in red (with wave images) and blue and yellow (without wave images). (**B**) Simulations were carried out with $c = 1.0$ and the slope of G randomly selected from a uniform probability distribution between −0.002 and 0.002 every 0.2 dimensionless time units, the interval between superimposed snapshots. Three different random walk trajectories for the same starting point are shown in red, blue, and yellow. The feedback parameters a and b in the experiments and simulations were the same as in Fig. 2. The scale bar in (A) is 2.0 mm.
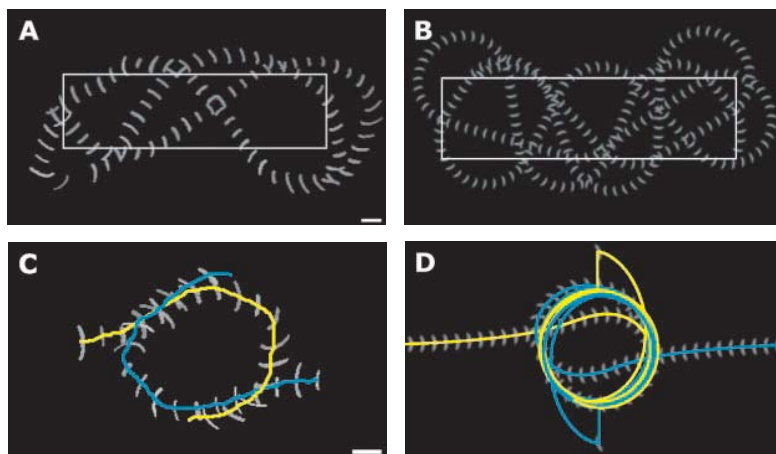
Fig. 4. Waves interacting with boundaries and with other waves. (**A**) Wave propagating in a gradient-free field, $G = 0$, and reflecting from barriers. As the wave crosses the barrier (indicated by the rectangle), the gradient is set to a constant value, $|grad(G)| = 0.75$, until it leaves the barrier region, where the gradient is again set to zero. The gain $c = 1.0$ and the time interval between snapshots is 40.0 s. (**B**) Simulations of waves reflecting from barriers (indicated by the rectangle), where the gradient is $|grad(G)| = 3.0 \times 10^{-4}$ in the barrier region. The gain $c = 1.0$ and the time interval between snapshots is 0.2 dimensionless time units. (**C**) Two propagating waves with mutual interaction according to Eqs. 1 and 3. The time interval between snapshots is 40.0 s, and the blue and yellow lines show the trajectory of each wave. The interaction strength is $c = 0.01$. (**D**) Simulations of waves with mutual interaction according to Eqs. 1 and 3. The time interval between snapshots is 0.2 dimensionless time units. The interaction strength is $c = 5.0 \times 10^{-6}$. The feedback parameters a and b in the experiments and simulations were the same as in Fig. 2. The scale bars in (A) and (C) are 2.0 mm.

boundary of the box, it experiences a constant gradient that is maintained perpendicular to its direction of propagation, which causes it to turn in a circular motion. The gradient is switched off when the wave reenters the box. Wave motion can therefore be confined to the box plus a boundary region with a width equal to twice the turning radius of the wave under the influence of the constant gradient. Other boundary-reflection rules (e.g., rules that describe realistic scattering angles) could be readily incorporated into the control algorithm.

Two waves "interacting" with each other are observed when attraction and repulsion terms are incorporated into the control algorithm. Experimental (Fig. 4C) and simulated (Fig. 4D) waves repel each other when they first approach and then become attracted to each other. Each wave was independently stabilized according to Eq. 1; however, now the gradient term is determined by the mutual orientation of the waves according to:

$$grad(G_i) = \hat{k}_i$$

$$\begin{cases} \left[\dfrac{d}{100} \theta_i + \dfrac{100}{d} (\theta_i - 180) \right], \theta_i \geq 0 \\[2mm] \left[\dfrac{d}{100} \theta_i + \dfrac{100}{d} (\theta_i + 180) \right], \theta_i < 0 \end{cases}$$

(3)

Here, $i = 1$ and 2 for waves 1 and 2, respectively; θ_i is the angle between the direction of propagation of each wave and the line connecting their centers of mass; d is the distance separating them; and $\hat{k}_i$ is a unit vector perpendicular to the velocity of the wave center. Both waves are governed by Eq. 3. When the interaction strength is the same for each wave ($c = 0.01$ in Eq. 1), they settle into a stable orbit, where their separation in the orbit is maximized. Figure 4D shows the wave trajectories for several orbits after the initial interaction between the waves (shown by the overlay of successive snapshots). Also shown are the waves relaxing back to the orbit after being perturbed away from the orbit, demonstrating that the orbit formed by the wave pair is stable.

Our experiments and simulations demonstrate how different modes of feedback can be combined to give patterns of spatiotemporal behavior that otherwise would not be possible. The primary feedback stabilizes waves that would not exist in the autonomous system. The wave-guiding excitability gradient, determined by the secondary feedback, permits a wide variety of wave patterns. This gradient represents a truly spatiotemporal feedback, as opposed to spatially homogeneous variations applied in global feedback. There is great flexibility in the design of spatiotemporal feedback, with the linear form used here being easily implemented but only the simplest possibility. Even the linear form, however, represents a dynamic combina-
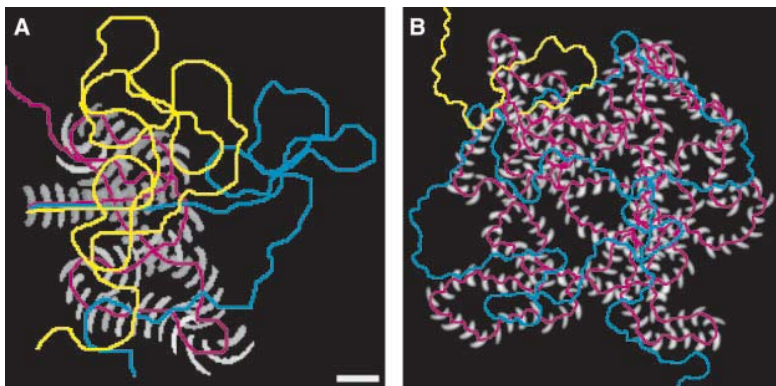
tion of positive and negative spatiotemporal feedback that is able to accurately direct wave propagation.

The control methods presented here also represent potential tools for investigating spatiotemporal dynamical systems. Our study has demonstrated that there is a direct proportionality between wave trajectory curvature and the excitability gradient for a given wave size (*24*). Control methods also provide a means for probing underlying mechanisms, as demonstrated in studies of homogeneous chemical systems (*25*, *26*). Such techniques are closely related to the relaxation methods developed by Eigen and co-workers (*27*) for probing chemical kinetics. Spatiotemporal behavior is pervasive in living systems, and control methods offer a promising direction for probing their underlying mechanisms.

References and Notes

1. M. Kim *et al.*, *Science* **292**, 1357 (2001).
2. J. Wolff, A. G. Papathanasiou, I. G. Kevrekidis, H. H. Rotermund, G. Ertl, *Science* **294**, 134 (2001).
3. V. Petrov, Q. Ouyang, H. L. Swinney, *Nature* **388**, 655 (1997).
4. A. L. Lin *et al.*, *Phys. Rev. E* **62**, 3790 (2000).
5. V. K. Vanag, L. Yang, M. Dolnik, A. M. Zhabotinsky, I. R. Epstein, *Nature* **406**, 389 (2000).
6. O. Steinbock, V. S. Zykov, S. C. Müller, *Nature* **366**, 322 (1993).
7. S. Grill, V. S. Zykov, S. C. Müller, *Phys. Rev. Lett.* **75**, 3368 (1995).
8. A. N. Zaikin, A. M. Zhabotinsky, *Nature* **225**, 535 (1970).
9. B. J. Gluckman, H. Nguyen, S. L. Weinstein, S. J. Schiff, *J. Neurosci.* **21**, 590 (2001).
10. L. Kuhnert, *Nature* **319**, 393 (1986).
11. E. Mihaliuk, T. Sakurai, F. Chirila, K. Showalter, *Faraday Discuss. Chem. Soc.* **120**, 383 (2002).
12. A fresh silica gel medium was prepared before each experiment by acidifying an aqueous solution of 10% (w/w) Na_2SiO_3 and 1.0×10^{-3} M $Ru(bpy)_3^{2+}$ with H_2SO_4. The gel was bathed in a catalyst-free BZ solution of 0.28 M $NaBrO_3$, 0.05 M malonic acid, 0.165 M bromomalonic acid, and 0.36 M H_2SO_4. The reaction mixture residence time and temperature were 4.5×10^2 s and 15.0°C. The spatial resolution of the camera and projector, each with an eight-bit gray level range, was 0.07 mm, and the time step for applying a new illumination pattern calculated from Eq. 1 was 2.0 s. The light at $\lambda = 460$ nm with a bandwidth $\Delta\lambda = 10$ nm had a maximum intensity ϕ, measured at the gel, of 0.5 mW/cm². Video camera measurements of gray levels $p(x, y)$ were obtained by interrupting the control algorithm for 0.1 s and applying a uniform illumination. The coordinates for the "center of mass" of a wave were calculated according to:

$$x_{cm} = \left[\sum_{x=1, y=1}^{n_x, n_y} (x \Theta[p(x, y) - p_{th}]) \right] / A$$

$$y_{cm} = \left[\sum_{x=1, y=1}^{n_x, n_y} (y \Theta[p(x, y) - p_{th}]) \right] / A$$

where x and y are spatial variables, n_x and n_y define the maximum size of the medium, $p(x, y)$ is the gray level, Θ is the Heaviside function giving 0 or 1 in the summations, and A is the wave area defined in Eq. 1.
13. Z. Noszticzius, W. Horsthemke, W. D. McCormick, H. L. Swinney, W. Y. Tam, *Nature* **329**, 619 (1987).
14. S. Kádár, T. Amemiya, K. Showalter, *J. Phys. Chem. A* **101**, 8200 (1997).
15. V. K. Vanag, A. M. Zhabotinsky, I. R. Epstein, *J. Phys. Chem. A* **104**, 8207 (2000).
16. I. Sendiña-Nadal, E. Mihaliuk, J. Wang, V. Pérez-Muñuzuri, K. Showalter, *Phys. Rev. Lett.* **86**, 1646 (2001).
17. R. H. Hooverman, *J. Appl. Phys.* **34**, 3505 (1963).
18. Numerical studies were carried out using an Oregonator model of the photosensitive BZ reaction (*19–21*): $[(\partial u)/(\partial t)] = D_u \nabla^2 u + [1/(\epsilon)](u - u^2 - (\phi + fv)[(u - q)/(u + q)])$, $[(\partial v)/(\partial t)] = u - v$, where u and v are the concentrations of $HBrO_2$ and $Ru(bpy)_3^{3+}$, and ϕ is the rate of photochemical production of Br^-. All simulations were carried out using the Crank-Nicholson method with parameters $f = 2.5$, $q = 0.0002$, $\epsilon = 0.01$, $D_u = 0.1$, the time step $dt = 0.001$, and the spatial grid $dx = 0.02$. Control of wave motion was carried out using Eq. 1 analogous to the experimental study, except that the wave area was determined by counting pixels with the variable u above a threshold value u_{th}.
19. R. J. Field, R. M. Noyes, *J. Chem. Phys.* **60**, 1877 (1974).
20. J. J. Tyson, P. C. Fife, *J. Chem. Phys.* **73**, 2224 (1980).
21. H. J. Krug, L. Pohlmann, L. Kuhnert, *J. Chem. Phys.* **94**, 4862 (1990).
22. G. Li, Q. Ouyang, V. Petrov, H. L. Swinney, *Phys. Rev. Lett.* **77**, 2105 (1996).
23. The control algorithm guides the wave along the target trajectory, generated by advancing the free parameter in Eq. 2. In the case where the trajectory intersects itself, we require the control algorithm to follow the advancing target trajectory.
24. F. Chirila, E. Mihaliuk, T. Sakurai, K. Showalter, in preparation.
25. A. Arkin, J. Ross, *J. Phys. Chem.* **99**, 970 (1995).
26. E. Mihaliuk, H. Skødt, F. Hynne, P. G. Sørensen, K. Showalter, *J. Phys. Chem. A* **103**, 8246 (1999).
27. M. Eigen, L. De Mayer, in *Technique of Organic Chemistry*, S. L. Friess, E. S. Lewis, A. Weissberger, Eds. (Interscience, New York, 1963), vol. 8 (no. 2), p. 895.
28. Supported by NSF grant number CHE-9974336 and the Office of Naval Research (grant number N00014-01-1-0596). K.S. thanks Alexander Mikhailov for his hospitality at the Fritz-Haber-Institut der Max-Planck-Gesellschaft and for many useful discussions that benefitted this study.

A Reversible Solid-State Crystalline Transformation in a Metal Phosphide Induced by Redox Chemistry

D. C. S. Souza,[1] V. Pralong,[1] A. J. Jacobson,[2] L. F. Nazar[1]*

We demonstrate low-potential intercalation of lithium in a solid-state metal phosphide. A topotactic first-order transition between different but related crystal structures at room temperature takes place by an electrochemical redox process: $MnP_4 \leftrightarrow Li_7MnP_4$. The P–P bonds in the MnP_4 structure are cleaved at the time of Li insertion (reduction) to produce crystalline Li_7MnP_4 and are reformed after reoxidation to MnP_4, thereby acting as an electron storage reservoir. This is an unusual example of facile covalent bond breaking within the crystalline solid state that can be reversed by the input of electrochemical energy.

Crystalline transformations in the solid state are kinetically hindered reactions that typically occur on geological time scales without the benefit of high temperature, owing to the difficulty of transport within the bulk. An exception is intercalation, where ions are inserted and extracted within gaps in low-dimensional lattices with no substantial change to the lattice itself (*1*). These processes can take place at ambient conditions because of the minimal restructuring involved. They form the basis on which lithium-ion batteries function—namely, simultaneous reversible (de)intercalation of lithium ions at both high-potential (positive) and low-potential (negative) electrodes (*2*). Although all positive materials operate on this principle, graphitic carbon, used commercially, is the only material to display classical intercalation behav-

ior at low potential (<1.0 V). $Li_4Ti_5O_{12}$ can intercalate one Li, but does so at a higher potential of 1.55 V (*3*). Other promising materials recently suggested for negative electrodes reversibly uptake lithium by other processes. These include alloying reactions in Li_xSn or Li_xSb nanophases (*4*, *5*), "uptake" by amorphous metal nitrides (*6*, *7*), and reduction to nanophasic metal or suboxide particles in metal oxides (*8*, *9*). Reaction of Li in the intermetallic phase Cu_6Sn_5 was reported to involve low-potential Li insertion involving Sn displacements within the lattice (*10*), although the breadth of the x-ray reflections made identification of the Li-rich phase ambiguous. Later evidence suggests that, during deep Li insertion, Sn is extruded from the lattice and Li-Sn alloying is responsible for Li uptake (*11*).

Here, we demonstrate low-potential intercalation behavior in a solid-state compound based on a metal phosphide. Phosphides lie between the more ionic nitrides and the intermetallic antimonides in their chemistry, but to date, little is known of their electrochemical behavior. We show that a topotactic first-order transition be

[1]Department of Chemistry and the Waterloo Centre for Materials Research, University of Waterloo, Waterloo, Ontario N2L 3G1, Canada. [2]Department of Chemistry, University of Houston, Houston, TX 77204, USA.

*To whom correspondence should be addressed. E-mail: lfnazar@uwaterloo.ca